

Fig. 10.1. A three-dimensional Gaussian wave packet moves freely in space. Its position expectation value moves on a straight line in the x,y plane. The first three illustrations show for three equidistant moments in time the probability density in the x,y plane as a bell-shaped surface, the expectation value as a dot on the plane, and the trajectory of the corresponding classical particle as a straight line in the plane. The covariance ellipse encircling the surface comprises a fixed fraction of the total probability. It contains the complete probability density information for the x,y plane. The complete information for the three-dimensional probability distribution is given by the probability ellipsoid. It is centered around the position expectation value and shown at the bottom for the three moments in time that are depicted separately in the first three plots. The classical trajectory in space is also shown.

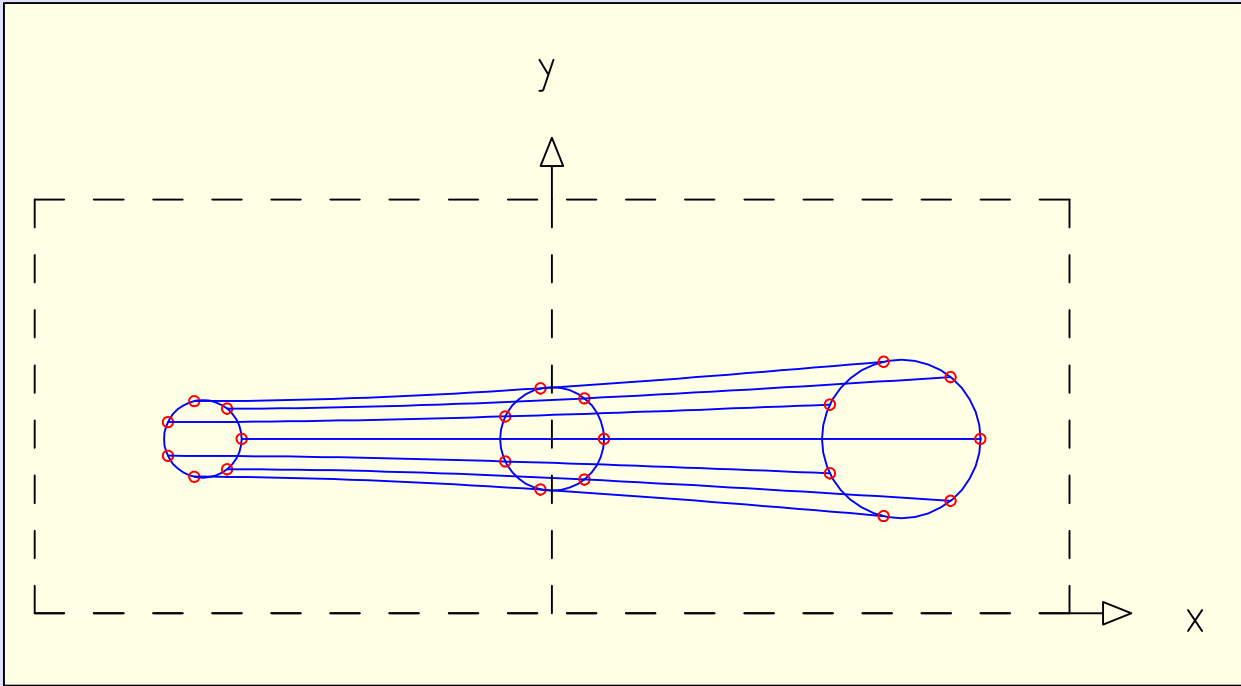


Fig. 10.2. The expectation value of a free three-dimensional spherically symmetric Gaussian wave packet, which initially (at time $t = t_0$) lies in the x, y plane, moves in the positive x direction. As initial volume V_0 comprising the probability P a sphere around the expectation value is chosen. Quantile trajectories $\vec{x}_P(t)$ of points which at $t = t_0$ lie on the surface of V_{t_0} at later times lie on the surface of volumes which also comprise the same probability P . In this simple example all volumes V_{t_i} are spheres. The plot shows the cuts $z = 0$ through three spheres V_0, V_{t_1}, V_{t_2} which are circles and trajectories in the x, y plane. All parameters are as in **Figure 10.1.**

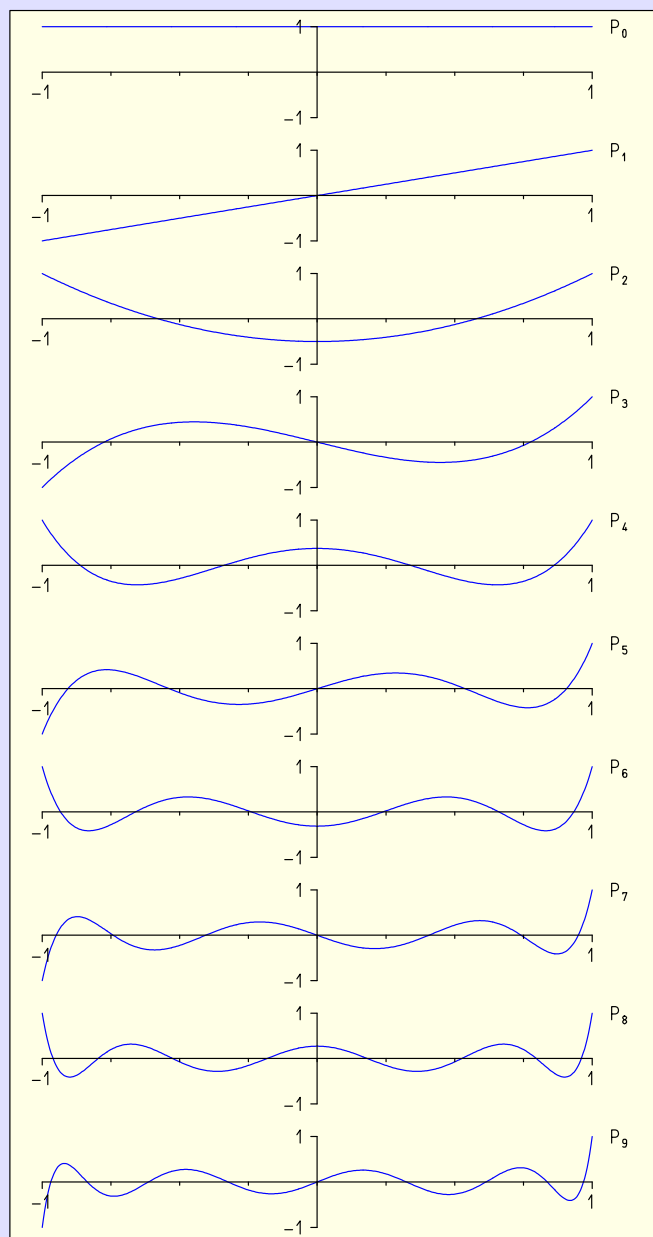


Fig. 10.3. The first ten Legendre polynomials $P_\ell(u) = \frac{1}{2^\ell \ell!} \frac{d^\ell}{du^\ell} [(u^2 - 1)^\ell]$.

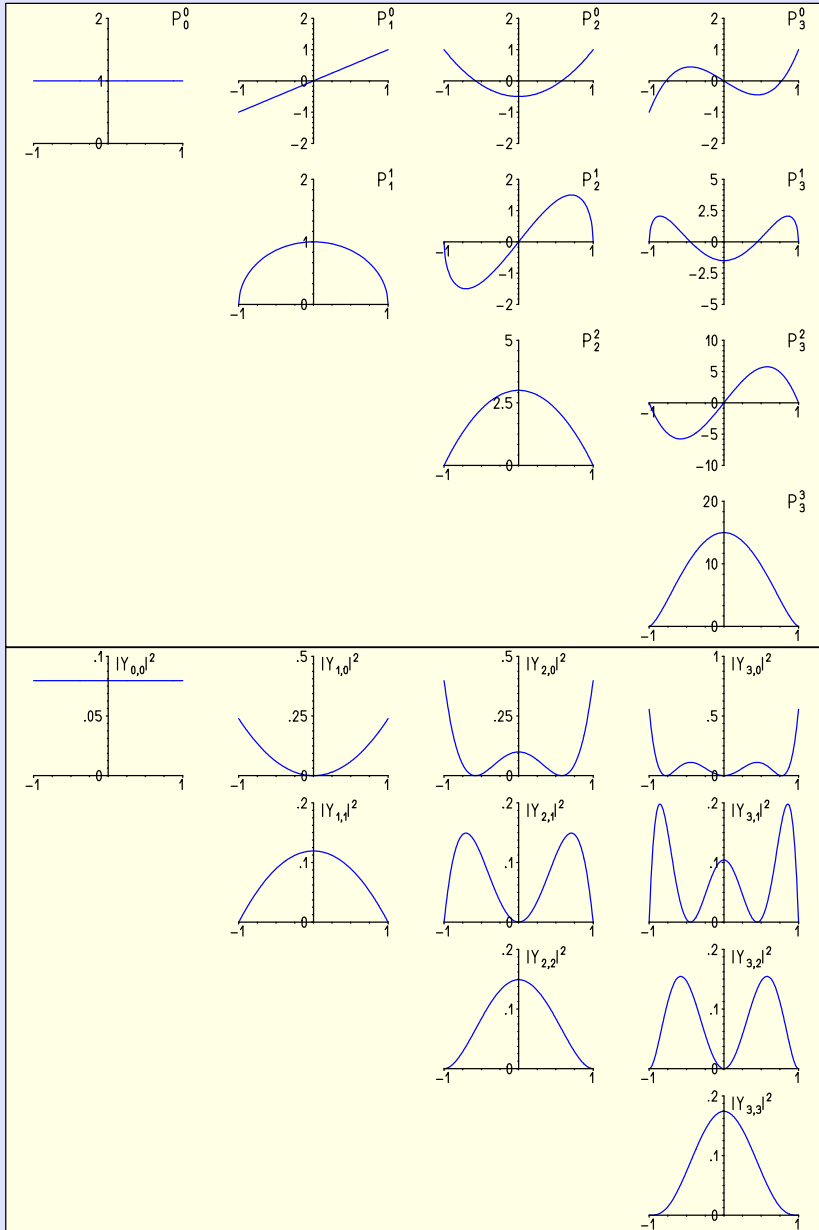


Fig. 10.4. Graphs of the associated Legendre functions $P_\ell^m(u)$, top, and of the absolute squares of the spherical harmonics $Y_{\ell m}(\vartheta, \phi)$, bottom. Except for a normalization factor, the absolute squares of the spherical harmonics are the squares of the associated Legendre functions.

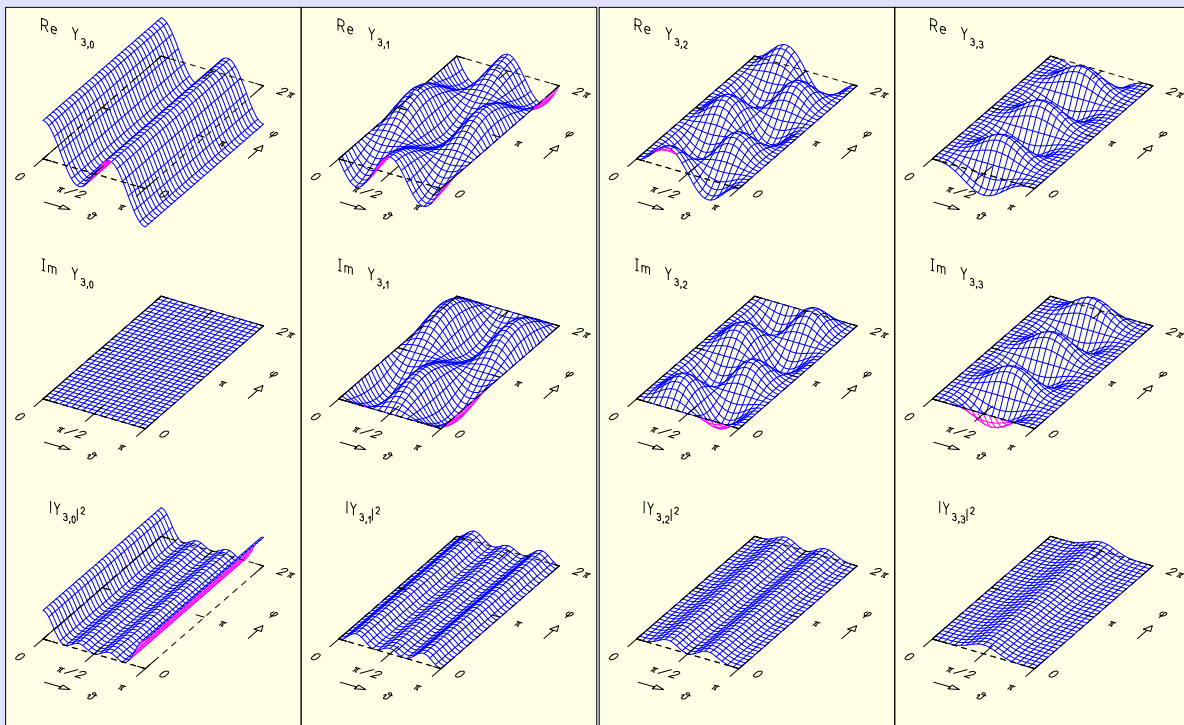


Fig. 10.5. The spherical harmonics $Y_{\ell m}$ are complex functions of the polar angle ϑ , with $0 \leq \vartheta \leq \pi$, and the azimuth ϕ , with $0 \leq \phi < 2\pi$. They can be visualized by showing their real and imaginary parts and their absolute square over the ϑ, ϕ plane. Such graphs are shown here for $\ell = 3$ and $m = 0, 1, 2, 3$.

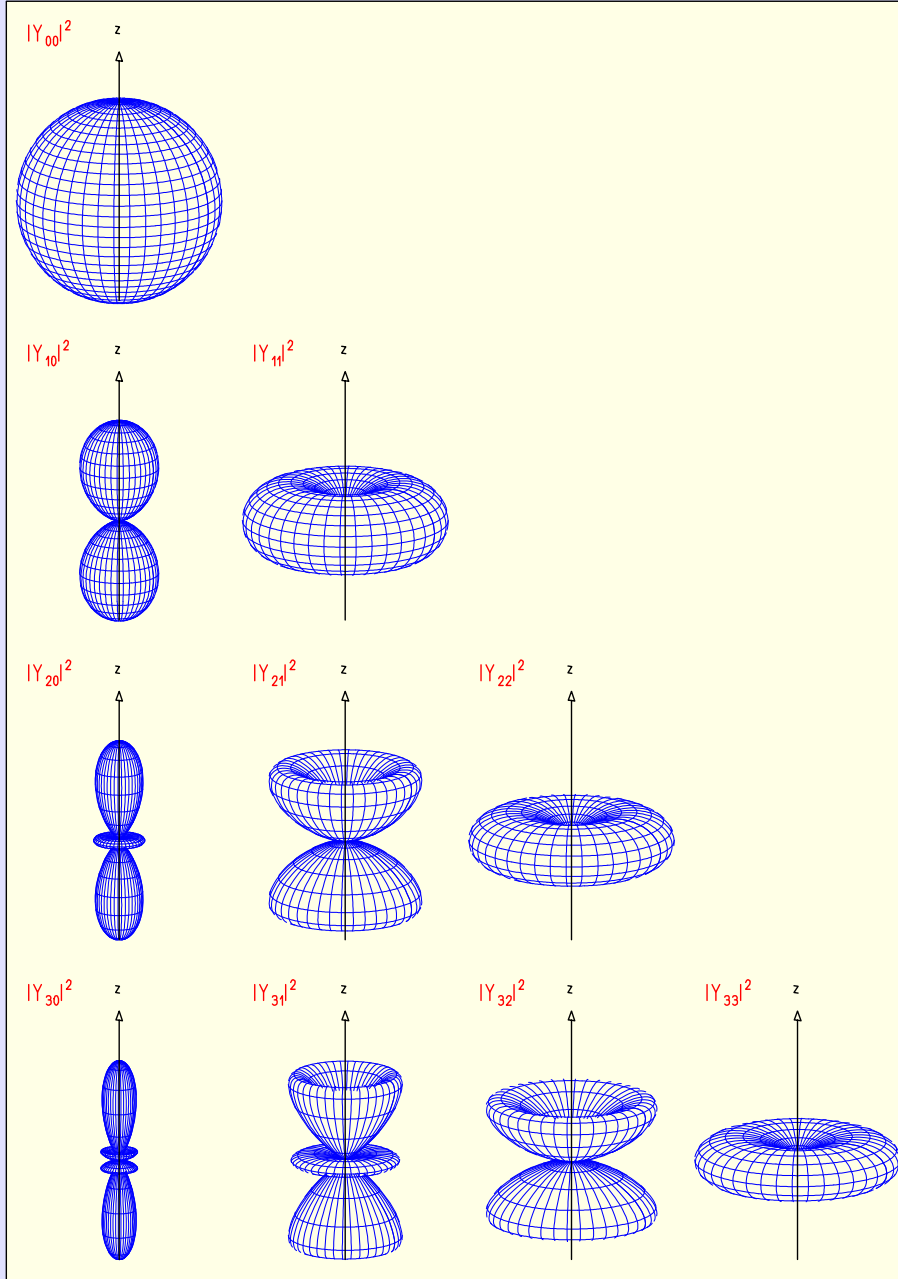


Fig. 10.6. Polar diagrams of the absolute squares of the spherical harmonics. The distance from the origin of the coordinate system to a point on the surface seen under the angles ϑ and ϕ is equal to $|Y_{\ell m}(\vartheta, \phi)|^2$. Different scales are used for the individual parts of the figure.

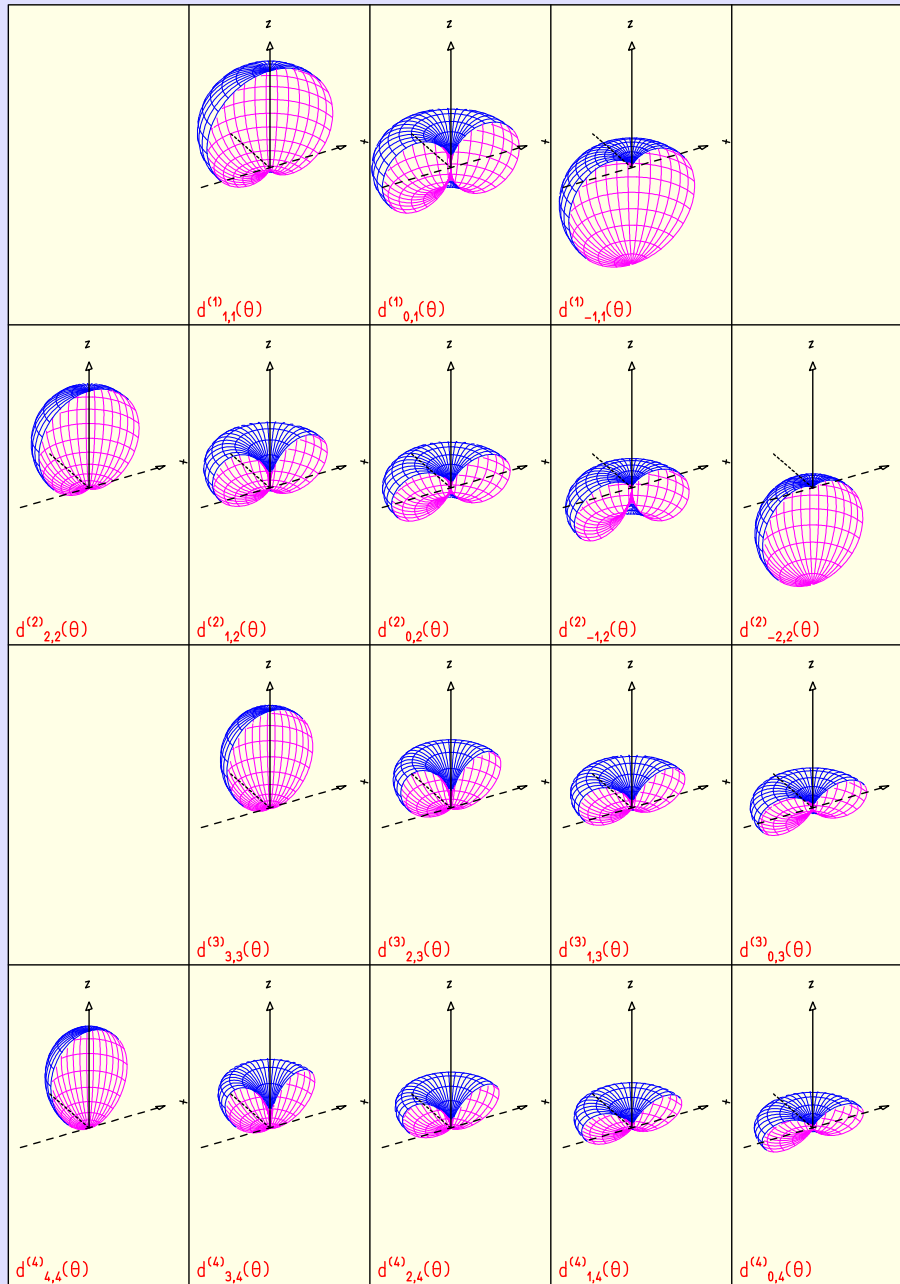


Fig. 10.7. Polar diagrams of the Wigner functions $d_{ml}^{(\ell)}(\theta)$. Lines 1 and 2 show the functions for $\ell = 1, 2$ and $m = \ell, \ell - 1, \dots, -\ell$. Lines 3 and 4 give them for $\ell = 3, 4$ and $m = \ell, \ell - 1, \dots, 0$. The functions are independent of Φ . They have large values only in a restricted region of θ . That region is near $\theta = 0$ for $m = \ell$ and decreases in regular steps via $\theta = \pi/2$ for $m = 0$ to $\theta = \pi$ for $m = -\ell$.

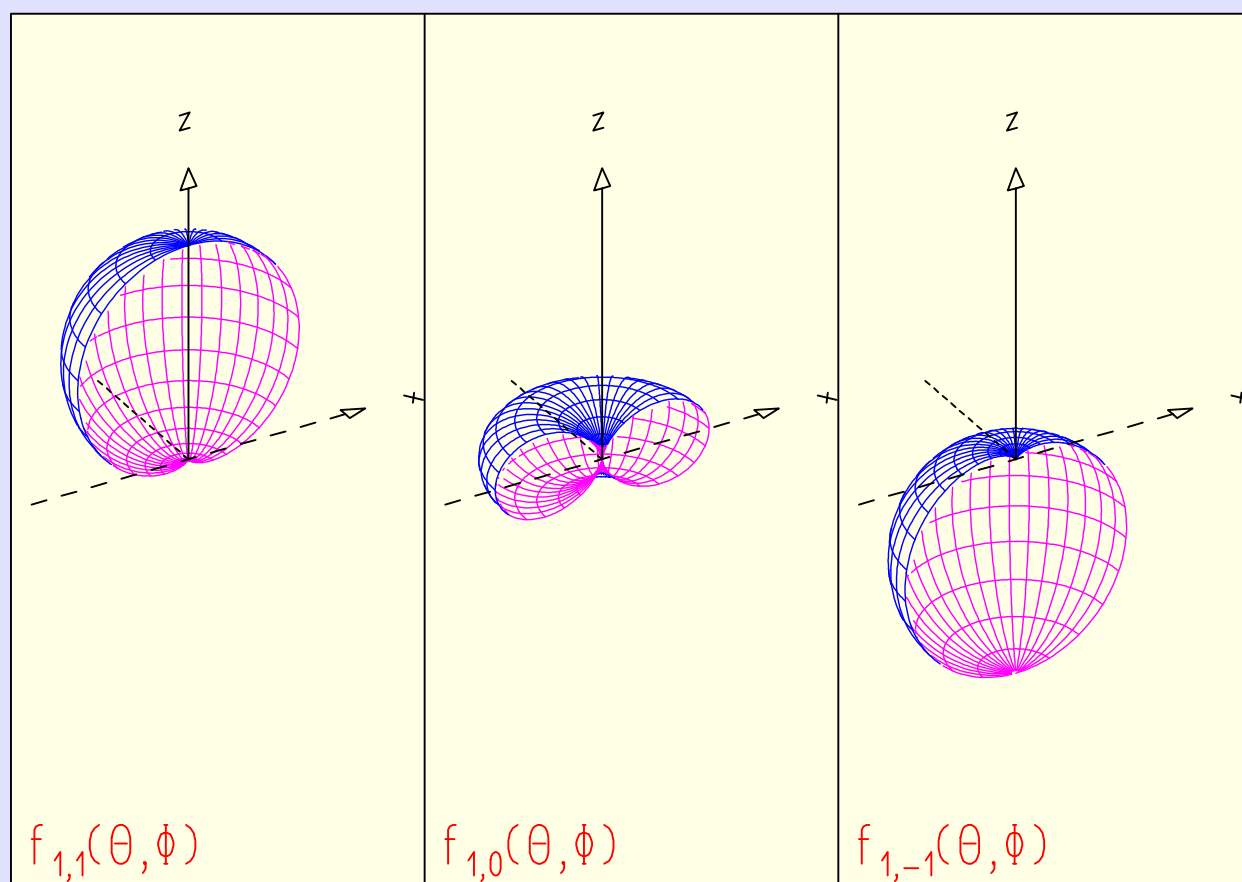


Fig. 10.8. Polar diagrams of the directional distributions $f_{\ell m}(\theta, \phi)$ for $\ell = 1$.

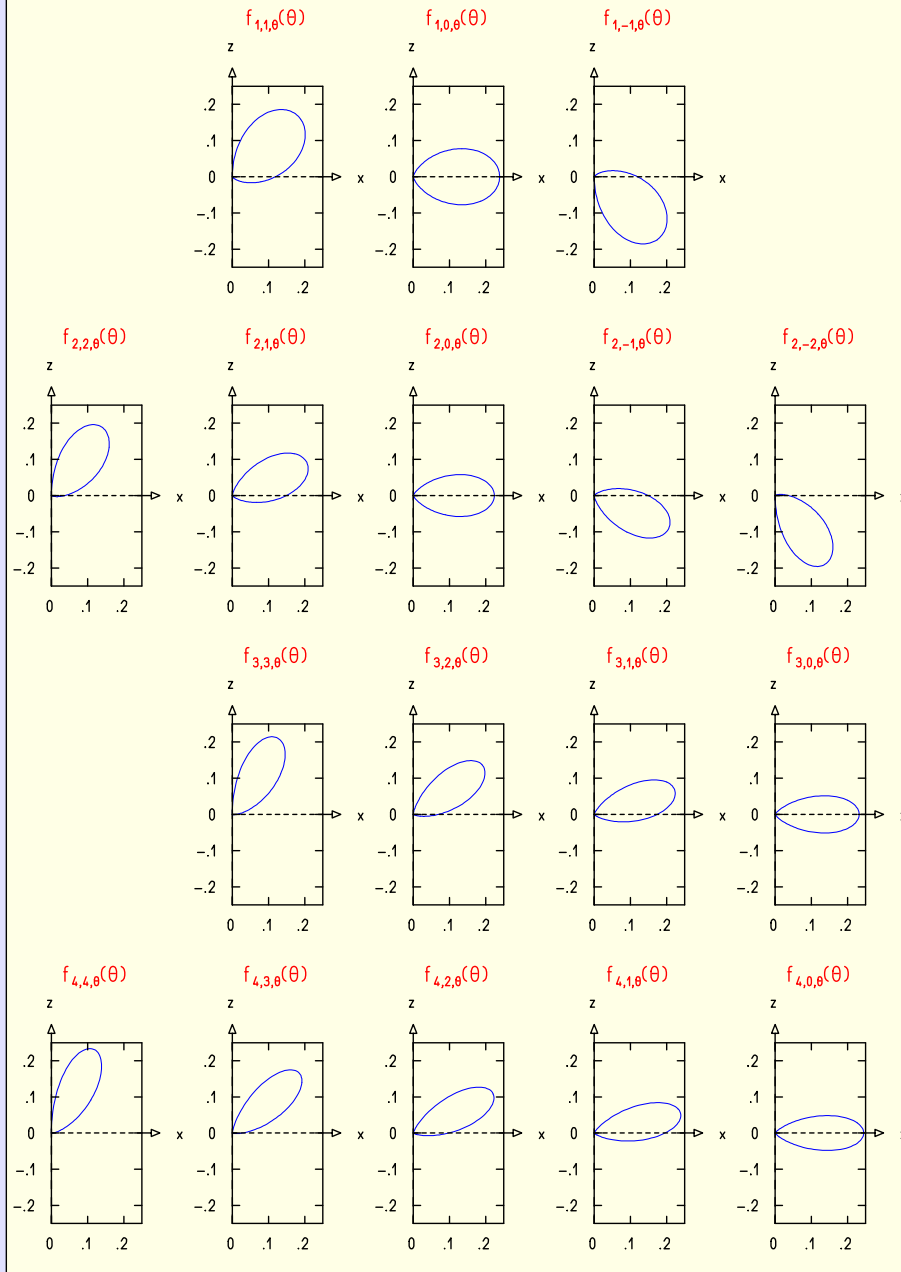


Fig. 10.9. Polar diagrams of the distribution $f_{\ell m \Theta}(\Theta)$ for the polar angle Θ of the direction of angular momentum. Lines 1 and 2 show the functions for $\ell = 1, 2$ and $m = \ell, \ell - 1, \dots, -\ell$. Lines 3 and 4 give them for $\ell = 3, 4$ and $m = \ell, \ell - 1, \dots, 0$.

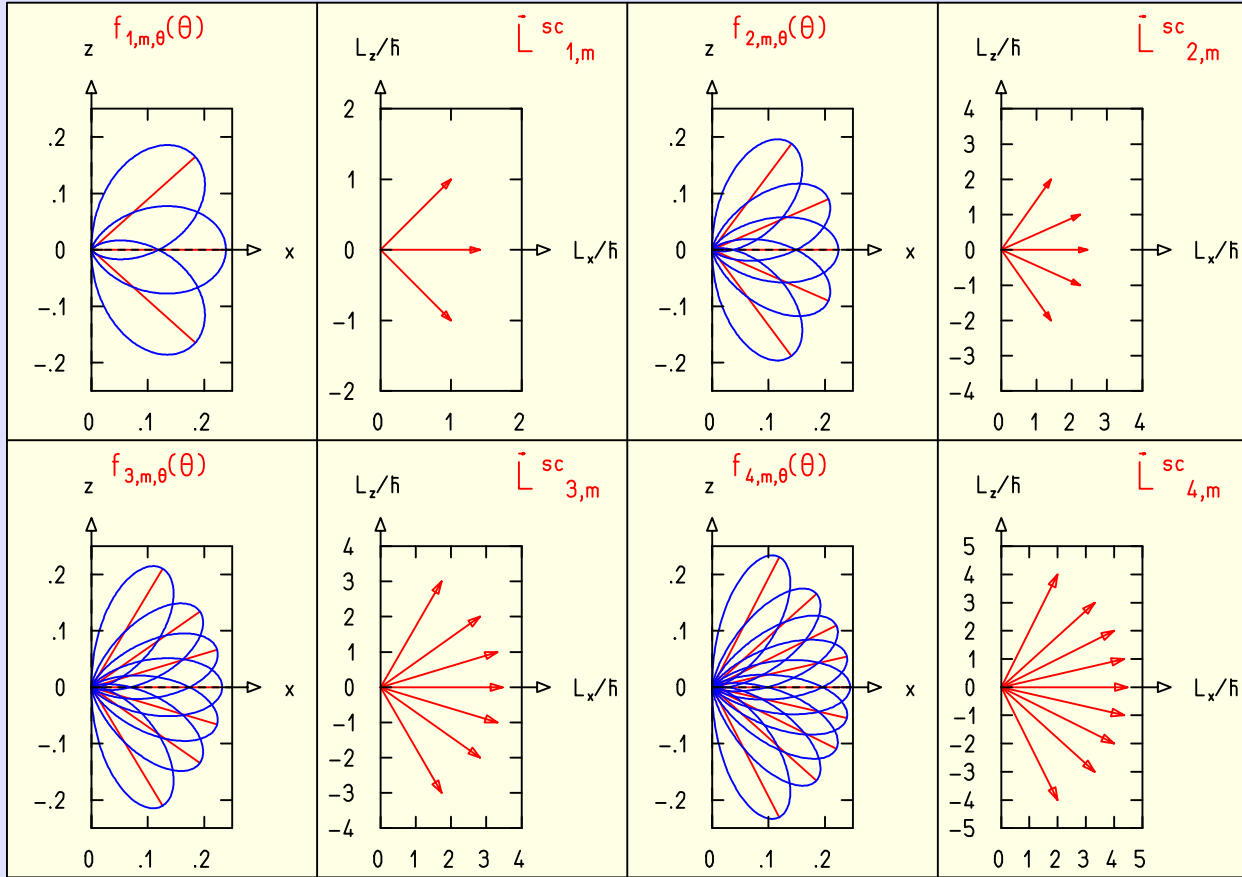


Fig. 10.10. Polar diagrams of the angular distribution $f_{\ell m \Theta}(\Theta)$. The top left plot contains all polar diagrams for $\ell = 1$. In addition each polar diagram contains a line from the origin to the point $f_{\ell m \Theta}(\Theta_{\ell m})$, where $\Theta_{\ell m}$ is the angle for which $f_{\ell m \Theta}$ has its maximum. The second plot from the left in the top row shows the semiclassical angular-momentum vectors $\vec{L}_{1,m}^{sc}$ which have polar angles similar to $\Theta_{\ell m}$. Pairs of plots of $f_{\ell m \Theta}(\Theta)$ and $\vec{L}_{\ell m}^{sc}$ are also shown for $\ell = 2, 3$, and 4.

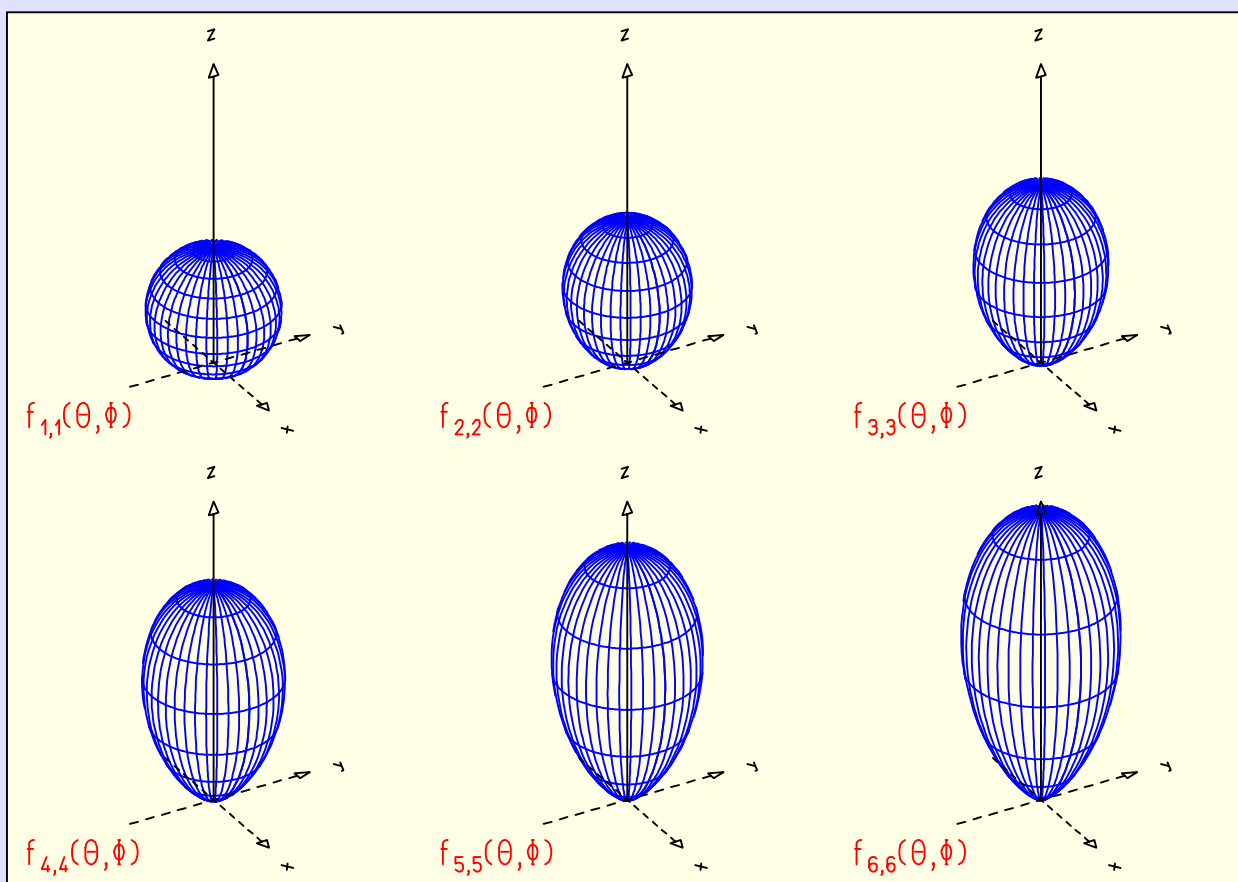


Fig. 10.11. Polar diagrams of the directional distribution $f_{\ell\ell}(\theta, \phi)$ for $\ell = 1, 2, \dots, 6$.

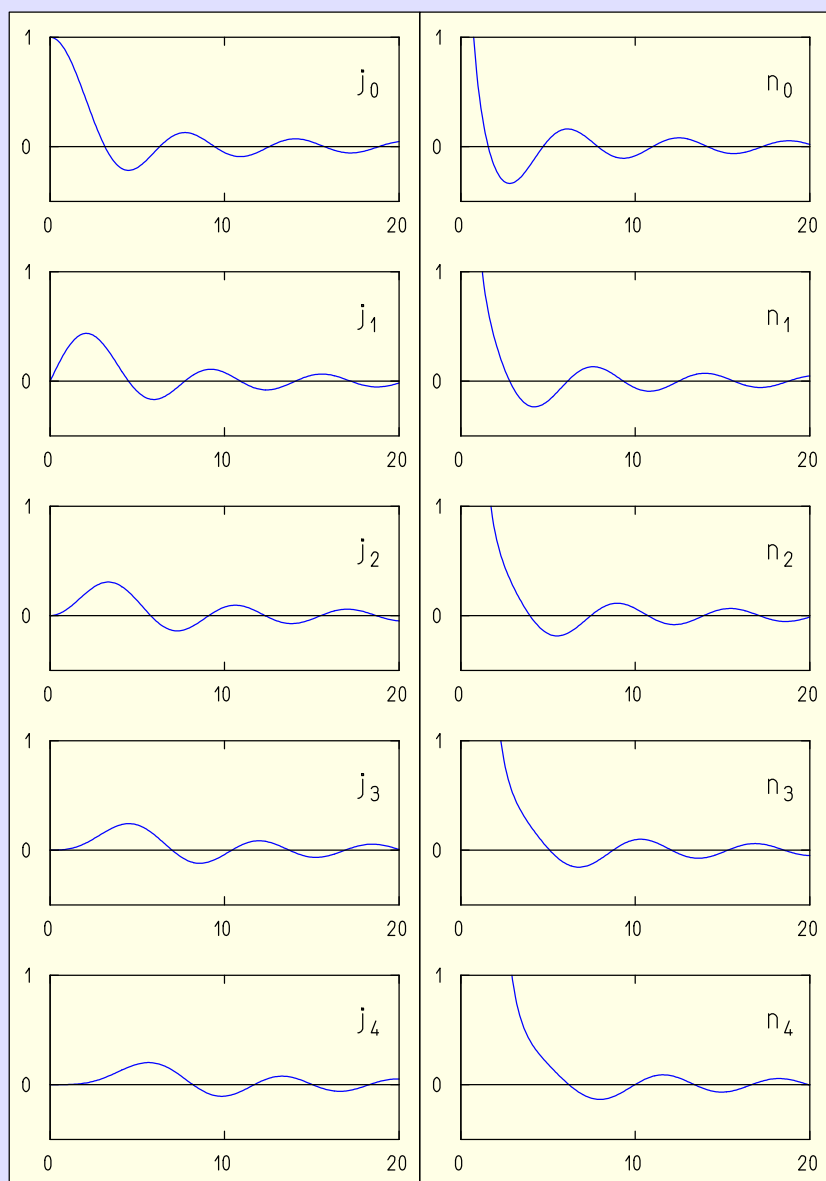


Fig. 10.12. Spherical Bessel functions $j_\ell(\rho)$ and spherical Neumann functions $n_\ell(\rho)$ for $\ell = 0, 1, \dots, 4$.

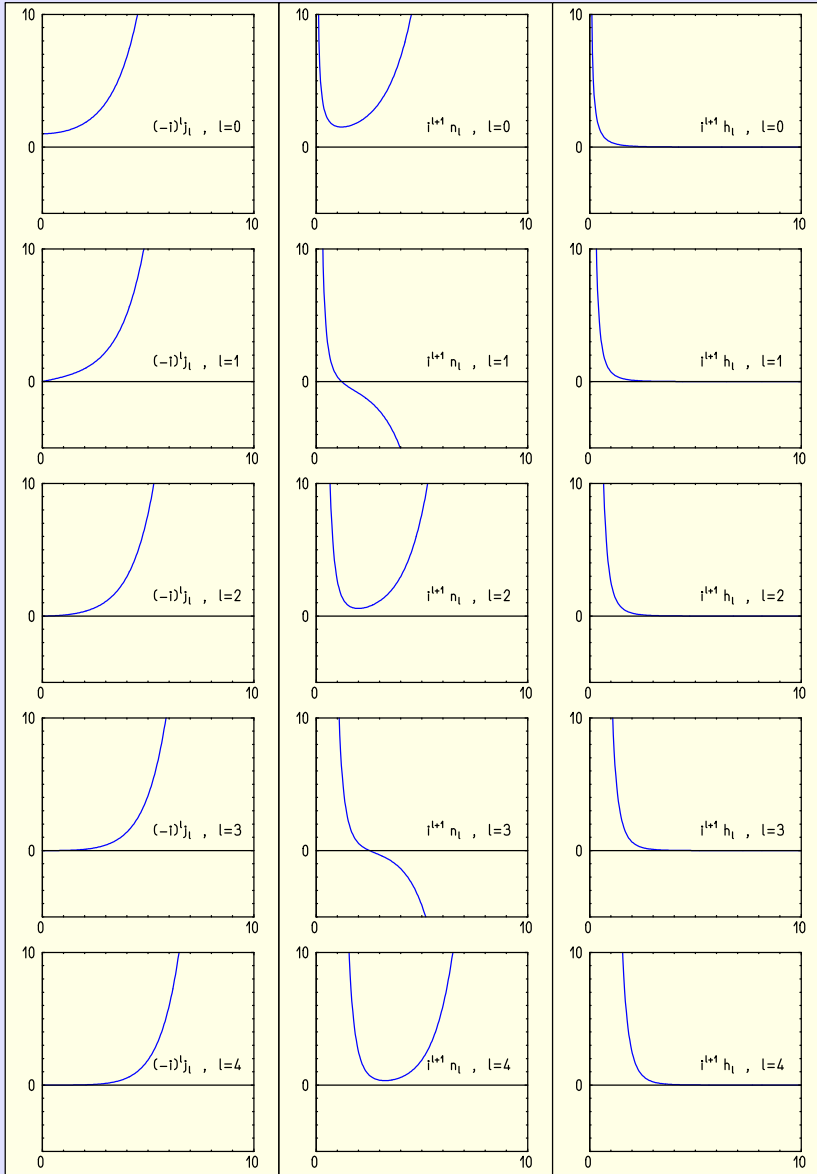


Fig. 10.13. For purely imaginary arguments $i\eta$, η real, the spherical Bessel functions j_ℓ , the spherical Neumann functions n_ℓ , and the spherical Hankel functions $h_\ell^{(+)}$ are either purely real or purely imaginary. The functions shown, that is, $(-i)^\ell j_\ell(\eta)$, $i^{\ell+1} n_\ell(\eta)$, and $i^{\ell+1} h_\ell^{(+)}(\eta)$, are purely real.

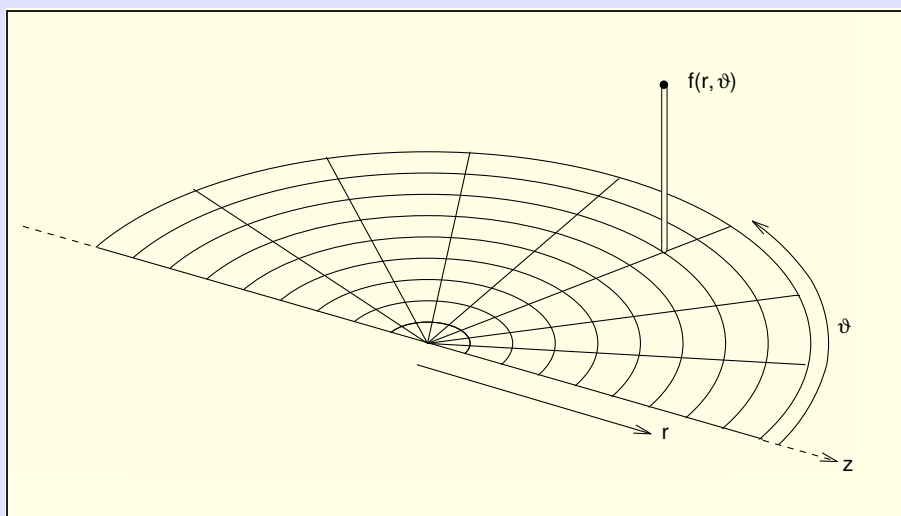


Fig. 10.14. The polar coordinate system used throughout the book for functions of the type $f = f(r, \vartheta)$. The admissible range of variables, $0 \leq r < \infty$, $0 \leq \vartheta \leq \pi$, corresponds to a half-plane. Here a half-circle around the origin, $r = 0$, is viewed perspectively from a point outside the half-plane. The polar angle ϑ is measured against the z axis, which points to the lower right. Lines of constant ϑ are straight lines beginning at the origin. Lines of constant r are half-circles. Using the direction perpendicular to the half-plane to define an f coordinate, we can represent a function $f(r, \vartheta)$ as a surface in r, ϑ, f space. Figures 10.15 and 10.16 show lines of constant r and constant ϑ on this surface.

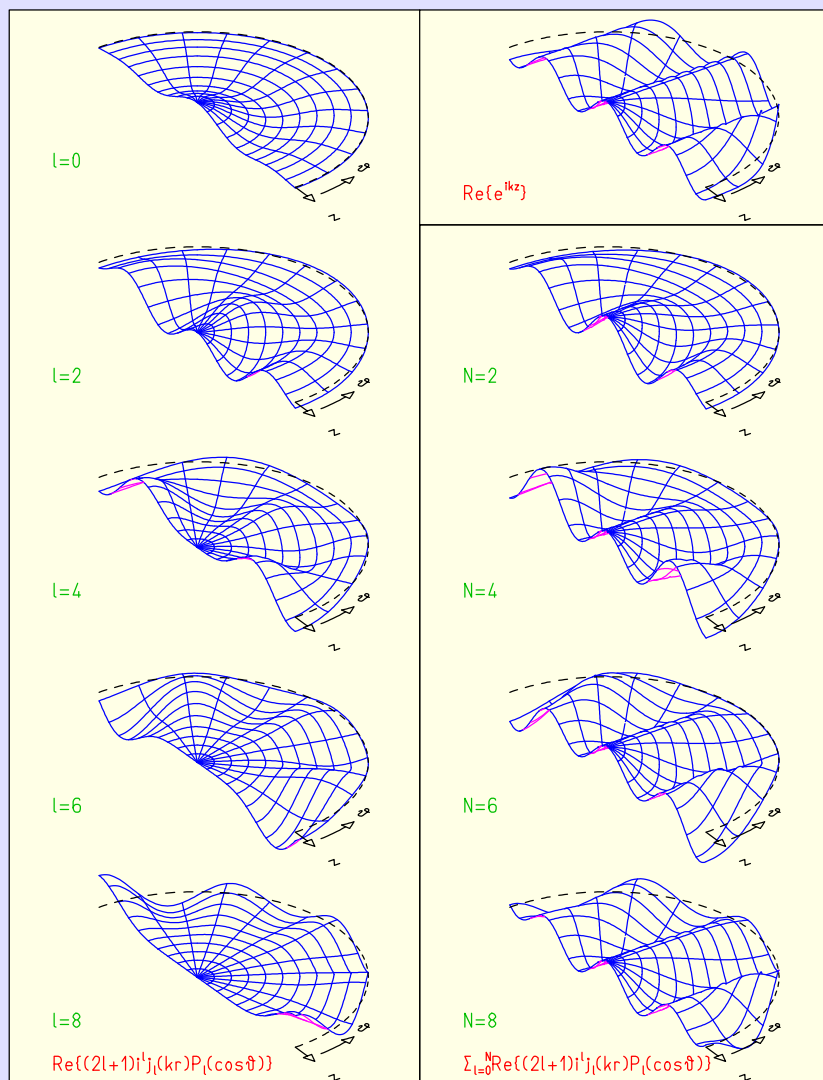


Fig. 10.15. Decomposition of a plane wave into spherical waves. The real part $\text{Re}\{e^{ikz}\} = \cos(kz)$ of a plane wave is shown in the top right corner. The left column contains the terms of the decomposition that are purely real. The right column contains the sums of the first two terms ($N = 2$), three terms ($N = 4$), and so on, of the left column.

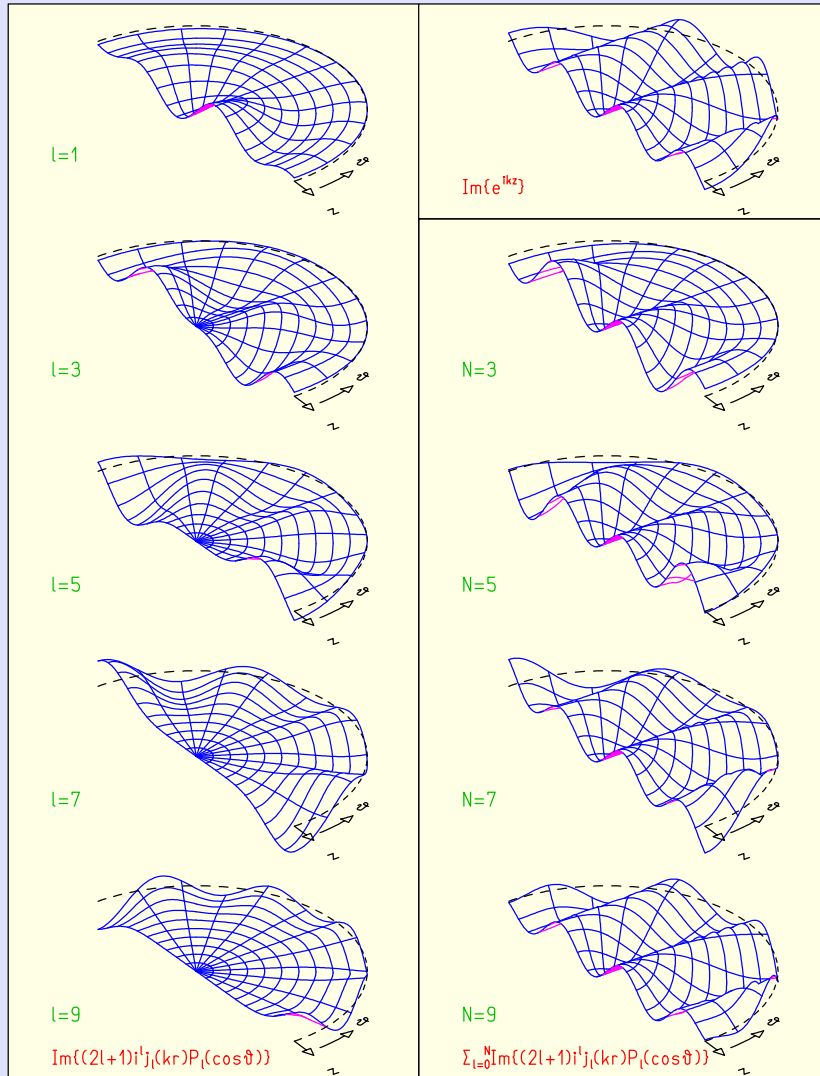


Fig. 10.16. Decomposition of a plane wave into spherical waves. The imaginary part $\text{Im}\{e^{ikz}\} = \sin(kz)$ of a plane wave is shown in the top right corner. The left column contains the terms of the decomposition that are purely imaginary. The right column contains the sums of the first two terms ($N = 3$), three terms ($N = 5$), and so on, of the left column.

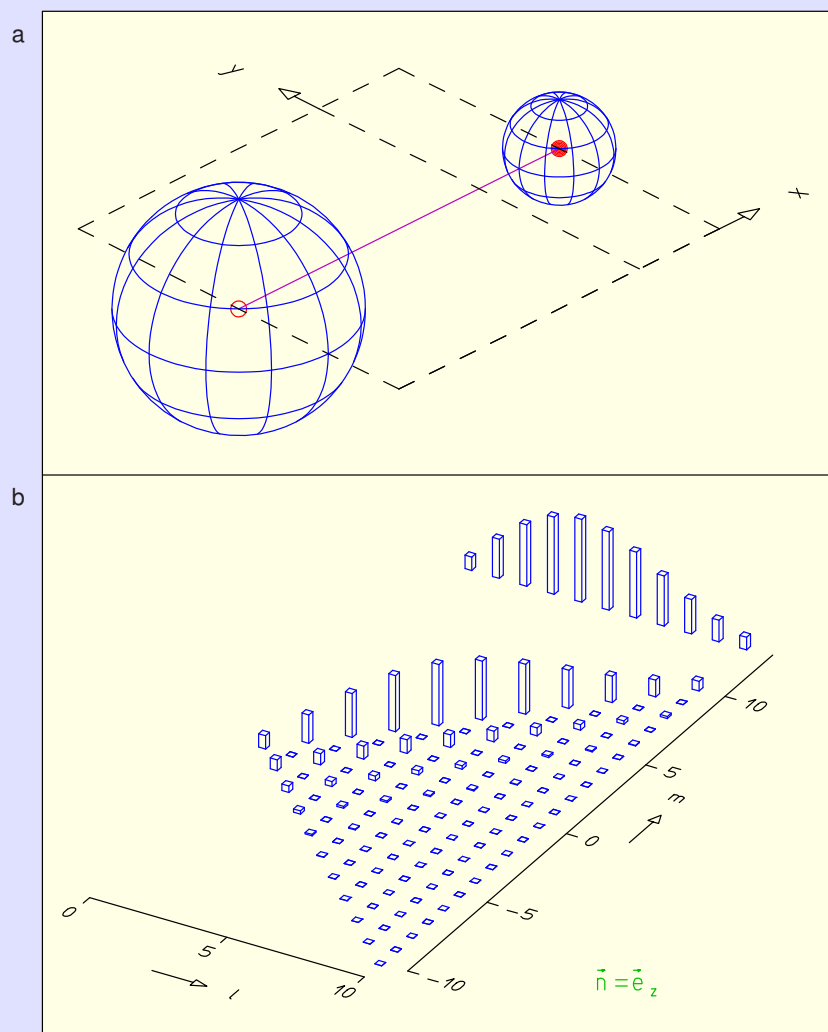


Fig. 10.17. (a) The probability ellipsoid, here a sphere, of a free wave packet moving in the x, y plane antiparallel to the x axis, shown at two moments of time. The dispersion of the wave packet is apparent through the growth of the sphere with time. (b) Decomposition of the wave packet shown in part a into angular-momentum states. The height of the column drawn at point (ℓ, m) is proportional to the probability $W_{\ell m}$ that the particle, which is described by the wave packet, has angular-momentum quantum number ℓ and quantum number m for the component of angular momentum along the quantization axis \vec{n} . In this figure \vec{n} was chosen to be the z axis. Also shown, on the upper margin, are the probabilities W_{ℓ} , that the particle possesses quantum number ℓ irrespective of the value of m .

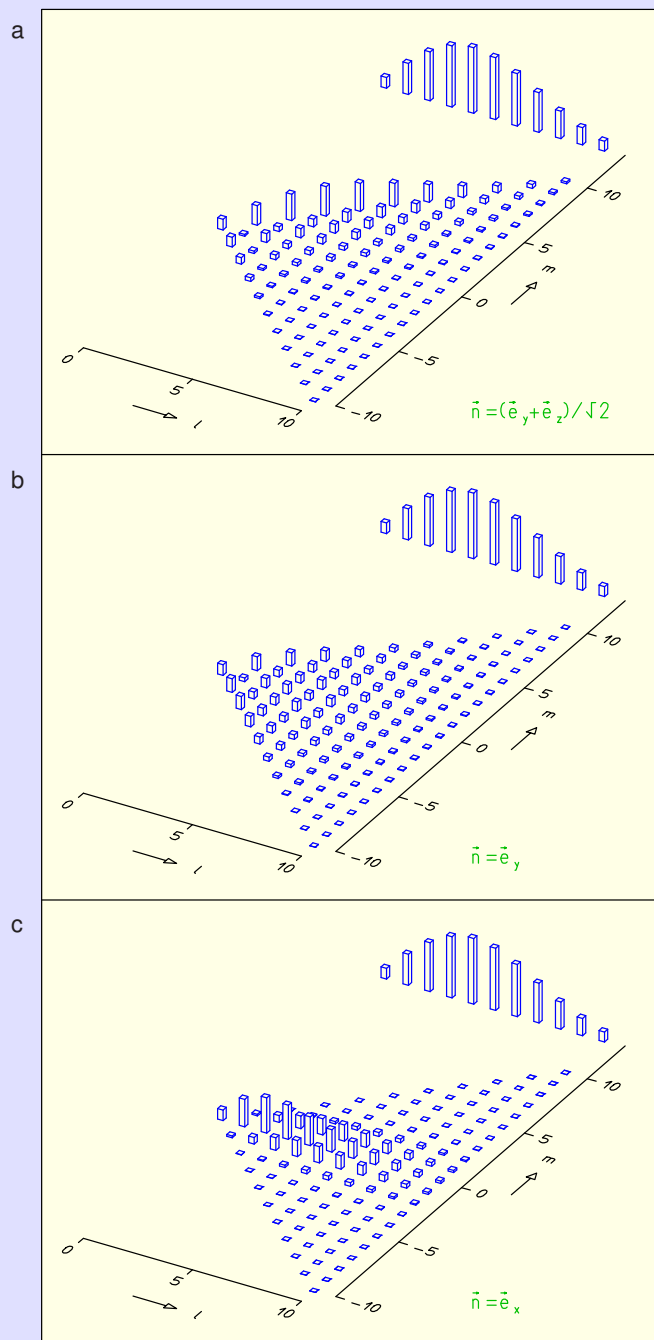


Fig. 10.18. All three figures apply to the situation of Figure 10.17a. Like Figure 10.17b, they show the decomposition of the wave packet into angular-momentum states. The quantization axes are different, however.